J. Fluid Mech. (2004), *vol.* 512, *pp.* 21–45.
DOI: 10.1017/S0022112004009139 Printed in the United Kingdom

Linear stability of Bingham fluids in spiral Couette flow

By JIE PENG AND KE-QIN ZHU

Department of Engineering Mechanics, Tsinghua University, Beijing, 100084, PRC

(Received 28 October 2002 and in revised form 25 November 2003)

The linear stability of Bingham-plastic fluid flow between two concentric cylinders rotating independently and with axial sliding of the inner cylinder (spiral Couette flow) is studied. Bingham fluid exhibits a yield stress in addition to the plastic viscosity, which has some inhibiting effects on the competition between the centrifugal and shear instability mechanisms owing to the inter-relationship of the azimuthal and axial velocities. Islands of instability, which are found in the spiral Couette flow of Newtonian fluids, may not exist owing to the effect of yield stress. The possibility of the yield surface falling between the cylinders is analysed. Although small perturbation waves appearing on the yield surface are considered, the yield surface, which has been treated as a free surface, has little effect on the flow stability. The effects of the axisymmetric and non-axisymmetric perturbation on flow stability are both presented. Both the rotation of the outer cylinder and a decrease of the gap between the cylinders have stabilizing effects.

1. Introduction

In the past century, hydrodynamic stability was recognized as one of the most difficult questions of fluid mechanics. The pioneering work was performed by Helmholtz, Kelvin, Rayleigh, Taylor, Reynolds, Orr, Sommerfeld and so on. To find why, when and how laminar flow breaks down into turbulent flow or some other laminar flows is still the target in this area. In this paper, the linear stability of Bingham-plastic fluid in spiral Couette flow is studied. It is a combination of the Taylor–Couette flow and the axial velocity field induced by the relative sliding.

This problem was first reported by Kiessling (1963) and Ludwieg (1964), who obtained inviscid stability criteria in the narrow-gap case. Up to now, the experiment of Ludwieg (1964) has been the only one on this topic. Later, Mott & Joseph (1968), Joseph & Munson (1970) and Hung, Joseph & Munson (1972) studied these general problems with energy methods. The importance of flow between coaxial cylinders as a fluid-dynamical paradigm has been well documented in the review by Diprima & Swinney (1981). The most interesting phenomenon of Taylor–Couette flow is the orderly progress of nonlinear flow states observed in the system as it undergoes transition to turbulence. The linear stability analysis of Newtonian spiral Couette flow has been studied by Ali & Weidman (1993) with a stationary outer cylinder and the inclusion of end effects. The general problem of oscillatory sliding of cylinders was studied by Hu & Kelly (1995) and Marques & Lopez (1997), whose results were in good agreement with those reported by Weisberg, Smits & Keverkidis (1997). Meseguer & Marques (2000) studied the competition between centrifugal and shear instability of Newtonian fluid in spiral Couette flow with open-ended configurations.

Islands of instability were found and explained as the results of the competition between the centrifugal and shear instability mechanism. An understanding of this problem could have applications in some industrial processes such as the purification of industrial waste water (Ollis, Pelizzetti & Serpone 1991), the production of paper (Cheng & Chang 1992) and wire and cable (Tadmor & Bird 1974) and the return flow of drilling mud between the rotating drill string and the stationary wall in oil and gas well drilling (Luo & Peden 1990; Cui & Liu 1995). For all of these, axial sliding in the cylindrical annulus combined with the rotation of one or both cylinders makes the stability characteristics and properties of the flow comparatively complex. Moreover, it is clear that the knowledge gained from these studies may be generally applicable to a wide range of much more complicated flows that demonstrate this type of instability.

Many recent studies of non-Newtonian flows have been concerned with viscoelastic and polymeric flows (Muller *et al.* 1989, 1993; Larson *et al.* 1990; Larson 1992; Joo & Shaqfeh 1992; 1994; Avgousti & Beris 1993; Nsom (1996, 1998); Al-Mubaiyedh, Sureshkumar & Khomami 2000). Shaqfeh (1996) reviewed purely elastic instabilities in viscometric flows and pointed out that the flows were simple, but critically important to the measurement devices common in the laboratories of rheologists and fluids engineers. Although there are a number of studies on the stability of Newtonian flows and viscoelastic (polymeric) flows, publications about viscoplastic flows are rare. Pascal & Rasmussen (1995) studied the stability of power-law-fluid flow between rotating cylinders. Coronado, Souza & Carvalho (2002) studied the critical Taylor number of viscoplastic fluids in the case of no imposed axial flow at different geometrical configurations, i.e. inner-to-outer cylinder radius ratio, and with different rheological parameters.

Bingham fluid is a type of yield stress fluid. Oldroyd (1947) formulated the constitutive relations between stress, strain and strain rate by assuming an elastic response below the yield stress. Generally, the elastic behaviour has been neglected and the constitutive equation can be written as (see Beris *et al.* 1985)

$$\left.\begin{array}{ll} \tau^* = \eta^* \dot{\gamma}^*, & \tau^* \geqslant \tau_0^*, \\ \dot{\gamma}^* = 0, & \tau^* < \tau_0^*, \end{array}\right\} \tag{1.1}$$

where τ^* is the deviatoric stress tensor, $\dot{\gamma}^*$ is the rate-of-strain tensor whose components are defined by

$$\dot{\gamma}_{ij}^* = u_{i,j}^* + u_{j,i}^*, \tag{1.2}$$

where u_i^* is the velocity field of the fluid. τ_0^* is the yield stress, $\tau^* = \sqrt{\tau_{ij}^* \tau_{ij}^*/2}$ is the second invariant of the deviatoric stress tensor and η^* is the effective viscosity which can be defined as

$$\eta^* = \mu_0^* + \tau_0^* \dot{\gamma}^{*-1}, \tag{1.3}$$

where $\dot{\gamma}^* = \sqrt{\dot{\gamma}_{ij}^* \dot{\gamma}_{ij}^*/2}$ is the second invariant of the rate-of-strain tensor and μ_0^* is the plastic viscosity. These equations show that in regions where the yield stress is not exceeded, the rate-of-strain tensor is identically zero. Hence, such regions would behave as a rigid solid. These regions are called unyielded or plug regions. The determination of possible unyielded regions in which no deformation occurs is still a difficulty in flow analysis of Bingham fluids. The interface of the yielded and unyielded region is called the yield surface and its position relates closely to the flow velocity. For this reason, Bingham fluid-flow problems are often interpreted as moving-boundary

problems which are more complex than the flow of Newtonian fluids. Bird, Dai & Yarusso (1983) reviewed analytical solutions for Bingham fluids in simple geometries.

Graebel (1962) studied the linear stability of a Couette–Taylor flow of a Bingham fluid. He considered the yield surface and presented the neutral stability curves. In summary, Graebel pointed out that the non-Newtonian factors involved in the flow of a Bingham fluid can be generally expected to be a stabilizing influence and the yield surface plays no role in the stability criterion. Frigaard, Howison & Sobey (1994) studied the linear stability of plane Poiseuille flow of a Bingham fluid, in which the unyielded region is considered able to maintain an initial infinitesimal perturbation persistently. So the disturbance of the yield surface has been taken into account. It is found that the minimum Reynolds number for linear instability increases almost linearly with increasing Bingham number which is defined as $\tau_0^* L/\mu_0^* U_0^*$. Here, L is the length scale and U_0^* is the velocity scale. Nsom & Mangel (2001) studied the stability of Taylor–Dean flow of the Bingham fluid. The effect of the yield stress on the velocity field is presented. The governing linear stability of the flow is produced with a small-gap approximation.

In this paper, the effects of the yield stress on the stability of spiral Couette flow were examined carefully. It is found that the azimuthal and axial velocities of the basic flow are interdependent owing to the existence of yield stress. In the absence of axial sliding, the Taylor–Couette flow can be reproduced. When yield stress is small, it causes instability in the co-rotating state with large outer rotation Reynolds number Re_0 and these results are very different to those of Graebel (1962). The stability analysis of spiral Couette flow shows that the competition between the centrifugal and axial shearing instability mechanisms, which are independent in Newtonian flows, can be effectively inhibited owing to the existence of the yield stress. The discontinuities in the critical inner rotation Reynolds number observed in the Newtonian flows can be eliminated while the yield stress is large. Corresponding research has, as far as we know not been presented.

The content of the paper is as follows. A complete physical and numerical description of the problem is given in § 2, and the analytical basic flow solutions are derived. In § 3, the linear differential equations about the linear stability of the first-order perturbations are obtained by using Galerkin approximation methods. In § 4, for each value of Re_o, Re_z and τ_0 (outer Reynolds number, axial Reynolds number and the non-dimensional yield stress, respectively) the numerical solutions are given. The numerical results for $\tau_0 = 0$ have been compared with those obtained by Sparrow, Munro & Jonsson (1964) and Meseguer & Marques (2000). The neutral stability curves are calculated. The 'islands' of stability, which appear in Newtonian spiral Couette flow, may not be observed. This phenomenon is explained in detail as the inhibiting effects of the yield stress on the competition between the centrifugal instability mechanism characteristic of the Taylor–Couette problem and the shear instability mechanism induced by the axial sliding. In § 5, our conclusions are presented.

2. Basic flow solution

As indicated above, spiral Couette flow is the term used to describe the combination of Taylor–Couette flow between two concentric rotating cylinders, whose radius and angular velocities are R_i^*, R_o^* and Ω_i^*, Ω_o^*, and the axial velocity field which was induced by the sliding of the inner cylinder with a constant velocity U_i^* (see figure 1). Apparently, more general flow with both cylinders moving axially can be reduced to the present case by changing to a reference frame with constant axial speed.

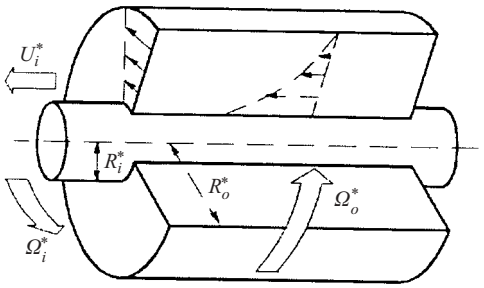

FIGURE 1. Geometric scketch and parameters of the spiral Couette flow.

Simon & Ole (1992) investigated a similar flow except that the axial flow was caused by the pressure gradient and the results were presented analytically for the slot approximation and numerically for the annulus. In this paper, the solution is found analytically without any approximation.

It can be seen that the geometry of the annulus, the yield stress and the azimuthal and axial velocities of the cylinders, which are independent of each other, do have influence on the instability of the flow. So the independent non-dimensional parameters chosen in this problem are: the radius ratio $\varepsilon = R_i^*/R_o^*$; the rotation Reynolds numbers $Re_i = \rho^* d^* R_i^* \Omega_i^*/\mu_0^*$ and $Re_o = \rho^* d^* R_o^* \Omega_o^*/\mu_0^*$, which describe the rotation speed of the inner and outer cylinders; the translational velocity of the inner cylinder is measured by the axial Reynolds number $Re_z = \rho^* d^* U_i^*/\mu_0^*$.

Hereinafter, all variables will be rendered dimensionless using d^*, $\rho^* d^{*2}/\mu_0^*$, $\mu_0^{*2}/d^{*2}\rho^*$ as units for space, time, pressure or stress. Generally, d^* can be chosen from R_i^*, R_o^*, $(R_i^* + R_o^*)/2$ or $R_o^* - R_i^*$ and we use $d^* = R_i^*$ here. The dimensionless continuity and momentum equations are

$$\nabla \cdot \boldsymbol{u} = 0, \tag{2.1}$$

$$\partial_t \boldsymbol{u} + (\boldsymbol{u} \cdot \nabla \boldsymbol{u}) = -\nabla p + \nabla \cdot \tau, \tag{2.2}$$

where the components of velocity $\boldsymbol{u}$ in cylinder coordinates (r, θ, z) are (u_r, u_θ, u_z). The dimensionless relative boundary conditions are

$$u_r(R_i) = u_r(R_o) = 0, \tag{2.3}$$

$$u_\theta(R_i) = Re_i, u_\theta(R_o) = Re_o, \tag{2.4}$$

$$u_z(R_i) = Re_z, u_z(R_o) = 0. \tag{2.5}$$

The dimensionless constitutive equation is

$$\left.\begin{array}{ll} \tau = \eta\dot{\gamma}, & \tau \geqslant \tau_0, \\ \dot{\gamma} = 0, & \tau < \tau_0, \end{array}\right\} \tag{2.6}$$

where $\eta = 1 + \tau_0 \dot{\gamma}^{-1}$ is the dimensionless effective viscosity, and $\tau_0 = \tau_0^* d^{*2} \rho^*/\mu_0^{*2}$ is the Hedstrom number which indicates the dimensionless yield stress. Assuming axisymmetric and infinite length of the cylinders along the axial, equation (2.1) can be satisfied naturally. In the most part, this work is concerned with the linear stability of the steady-state flow. The steady-state equation (2.2) can be simplified as

$$\frac{\partial \bar{\tau}_{r\theta}}{\partial r} + 2\frac{\bar{\tau}_{r\theta}}{r} = 0, \tag{2.7}$$

$$\frac{\partial \bar{\tau}_{rz}}{\partial r} + \frac{\bar{\tau}_{rz}}{r} = 0. \tag{2.8}$$

Through integration, (2.7) and (2.8) can be derived as

$$\bar{\tau}_{r\theta} = A/r^2, \tag{2.9}$$

$$\bar{\tau}_{rz} = B/r, \tag{2.10}$$

where A and B are constants. According to (2.6), the Bingham fluid remains unyielded when $\bar{\tau}_{r\theta}^2 + \bar{\tau}_{rz}^2 < \tau_0^2$. So from (2.9) and (2.10), it is obvious that if the yield surface generates in the gap between the concentric cylinders, the Bingham fluid outside the yield surface is in rigid-body rotation. Substituting (2.6) into (2.9), (2.10) and combining with the expressions of strain rate, we have

$$\frac{\partial \bar{u}_\theta}{\partial r} - \frac{\bar{u}_\theta}{r} - \frac{A}{r^2} + \frac{\tau_0 A}{\sqrt{A^2 + B^2 r^2}} = 0, \tag{2.11}$$

$$\frac{\partial \bar{u}_z}{\partial r} - \frac{B}{r} + \frac{r\tau_0 B}{\sqrt{A^2 + B^2 r^2}} = 0, \tag{2.12}$$

and the boundary conditions become

$$\bar{u}_\theta(R_i) = Re_i, \bar{u}_\theta(R_y) = Re_o \frac{R_y}{R_o}, \tag{2.13}$$

$$\bar{u}_z(R_i) = Re_z, \bar{u}_z(R_y) = 0. \tag{2.14}$$

R_y is the position of the yield surface which is unknown before the settlement of the problem. According to equations (2.6), (2.9) and (2.10), the condition satisfying the yield surface can be written as

$$\Phi(R_y) = \frac{1}{R_y}\sqrt{\frac{A^2}{R_y^2} + B^2} = \tau_0. \tag{2.15}$$

The distribution of the velocity, the yielded and unyielded regions are determined by the set of equations (2.11)–(1.15). The expressions of basic flow velocity $(0, \bar{u}_\theta, \bar{u}_z)$ can be derived and classified according to the motion of the cylinders:

(i) $Re_o/R_o = Re_i/R_i$ and $Re_z = 0$. The inner and outer cylinders rotate synchronously and the inner cylinder is stationary along the axial direction. The velocity expressions are

$$\bar{u}_\theta = Dr, \tag{2.16a}$$

$$\bar{u}_z = 0, \tag{2.16b}$$

where parameter $D = Re_o/R_o = Re_i/R_i$. In this case, all Bingham fluid in the gap between the cylinders remains unyielded and rotates just like the rotation of a rigid body. So, it maintains stabilization constantly.

(ii) $Re_o/R_o \neq Re_i/R_i$ and $Re_z = 0$. The inner cylinder is stationary along the axial direction. The velocity expressions are

$$\bar{u}_\theta = Dr - \frac{A}{2r} - \frac{\tau_0 A}{\sqrt{A^2}} r \ln r, \tag{2.17a}$$

$$\bar{u}_z = 0, \tag{2.17b}$$

where A and D can be determined by both the boundary conditions

$$DR_i - \frac{A}{2R_i} - \frac{\tau_0 A}{\sqrt{A^2}} R_i \ln R_i = Re_i, \tag{2.17c}$$

$$DR_y - \frac{A}{2R_y} - \frac{\tau_0 A}{\sqrt{A^2}} R_y \ln R_y = Re_o \frac{R_y}{R_o}, \tag{2.17d}$$

and the yield surface condition

$$\sqrt{\frac{A^2}{R_y^2}} = \tau_0 R_y, \tag{2.17e}$$

where R_y is the position of the yield surface which is unknown before the settlement of the problem. Bird, Armstrong & Hassager (1977) have studied the tangential annular flow of Bingham fluid caused by the rotation of the outer cylinder, while the inner cylinder is held fixed. The results can be reproduced by setting $Re_i = 0$ in (2.17c).

(iii) $Re_o/R_o = Re_i/R_i$ and $Re_z \neq 0$. The inner and outer cylinders rotate synchronously while the inner cylinder slides along the axial direction. The velocity expressions are

$$\bar{u}_\theta = Dr, \tag{2.18a}$$

$$\bar{u}_z = -\frac{\tau_0 B}{\sqrt{B^2}} r + B \ln r + C, \tag{2.18b}$$

and B, C and D can be determined by the boundary conditions

$$DR_i = Re_i, \tag{2.18c}$$

$$-\frac{\tau_0 B}{\sqrt{B^2}} R_i + B \ln R_i + C = Re_z, \tag{2.18d}$$

$$-\frac{\tau_0 B}{\sqrt{B^2}} R_y + B \ln R_y + C = 0, \tag{2.18e}$$

and the yield surface condition

$$\sqrt{B^2} = \tau_0 R_y. \tag{2.18f}$$

(iv) $Re_o/R_o \neq Re_i/R_i$ and $Re_z \neq 0$. The velocity expressions are

$$\bar{u}_\theta = Dr - \frac{A}{2r} - \frac{r\tau_0 A}{\sqrt{A^2}} \ln\left(\frac{\sqrt{A^2 + B^2 r^2} - \sqrt{A^2}}{r}\right), \tag{2.19a}$$

$$\bar{u}_z = -\frac{\tau_0}{B}\sqrt{A^2 + B^2 r^2} + B \ln r + C, \tag{2.19b}$$

and A, B, C and D can be determined by the boundary conditions

$$DR_i - \frac{A}{2R_i} - \frac{R_i \tau_0 A}{\sqrt{A^2}} \ln\left(\frac{\sqrt{A^2 + B^2 R_i^2} - \sqrt{A^2}}{R_i}\right) = Re_i, \tag{2.19c}$$

$$-\frac{\tau_0}{B}\sqrt{A^2 + B^2 R_i^2} + B \ln R_i + C = Re_z, \tag{2.19d}$$

$$DR_y - \frac{A}{2R_y} - \frac{R_y \tau_0 A}{\sqrt{A^2}} \ln\left(\frac{\sqrt{A^2 + B^2 R_y^2} - \sqrt{A^2}}{R_y}\right) = Re_o \frac{R_y}{R_o}, \tag{2.19e}$$

$$-\frac{\tau_0}{B}\sqrt{A^2 + B^2 R_y^2} + B \ln R_y + C = 0, \tag{2.19f}$$

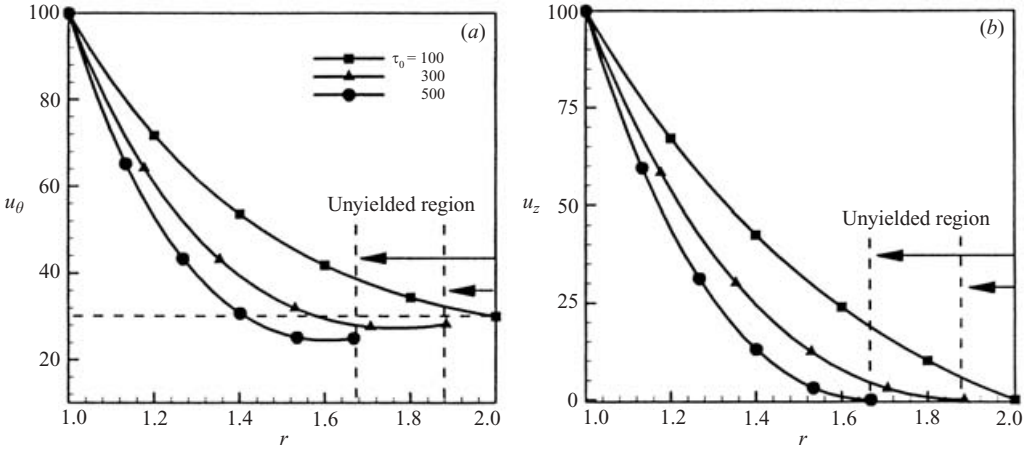

FIGURE 2. Velocity profiles with different Hedstrom number while $\varepsilon = 0.5$, $Re_i = 100$, $Re_o = 30$ and $Re_z = 100$. (*a*) Azimuthal velocity profiles. (*b*) Axial velocity profiles.

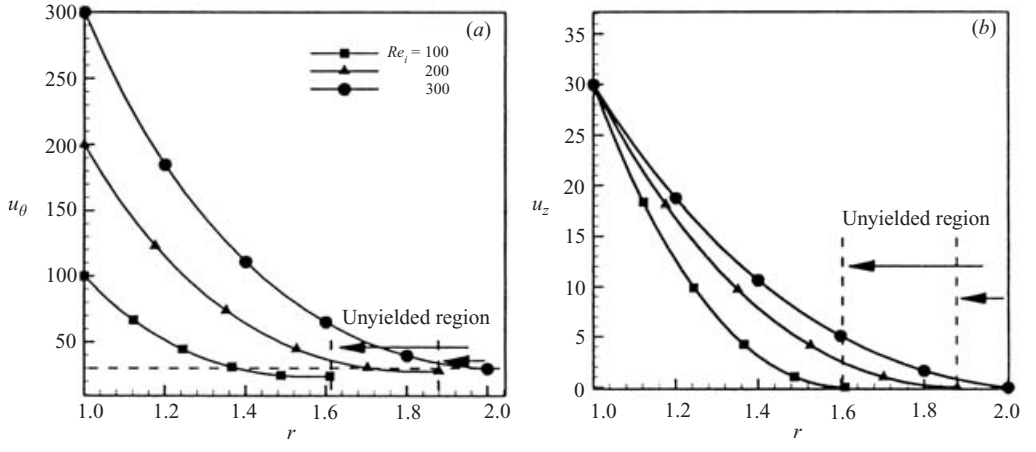

FIGURE 3. Velocity profiles with different Re_i while $\varepsilon = 0.5$, $Re_o = 30$, $Re_z = 30$ and $\tau_0 = 300$. (*a*) Azimuthal velocity profiles. (*b*) Axial velocity profiles.

and the yield surface condition

$$\frac{1}{R_y}\sqrt{\frac{A^2}{R_y^2} + B^2} = \tau_0. \tag{2.19g}$$

It must be pointed out that whether there are unyielded regions or not, the velocity expressions listed above are valid. If all Bingham fluid in the gap has been yielded, R_y should be replaced by R_o and the yield surface condition should be ignored.

The velocity profiles are shown in figure 2 with different values of Hedstrom number τ_0. It can be seen that the unyielded region enlarges and the velocity profile becomes more steep with increasing Hedstrom number. The azimuthal and axial velocity profiles are coupled, in contrast to those in Newtonian spiral Couette flow, because of the existence of yield stress. Figures 3 and 4 show the velocity profiles with

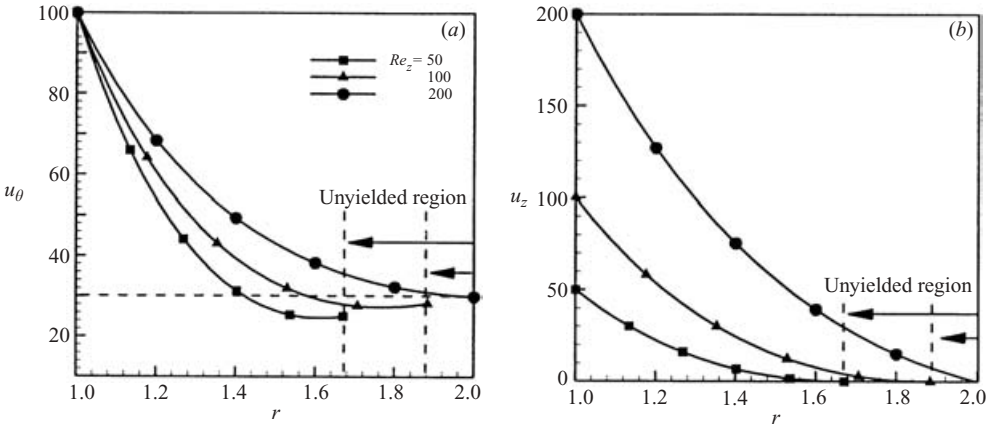

FIGURE 4. Velocity profiles with different Re_z while $\varepsilon = 0.5$, $Re_i = 100$, $Re_o = 30$ and $\tau_0 = 300$. (*a*) Azimuthal velocity profiles. (*b*) Axial velocity profiles.

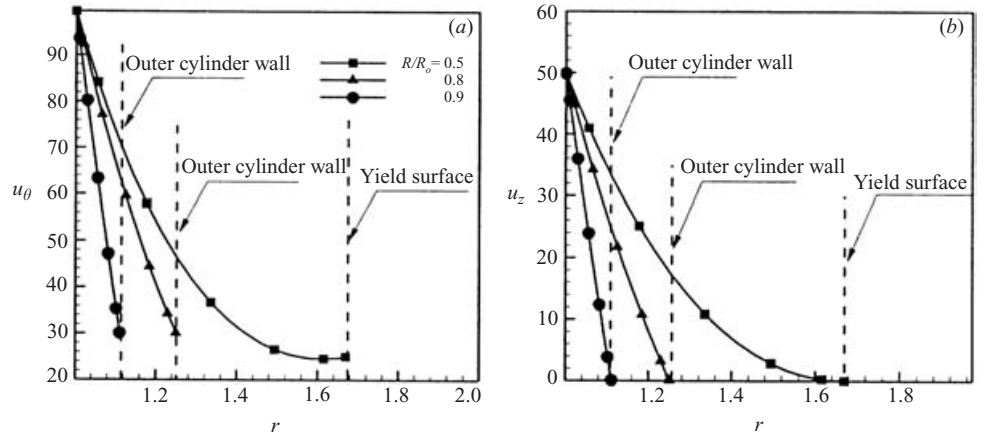

FIGURE 5. Velocity profiles with different ε while $Re_i = 100$, $Re_o = 30$, $Re_z = 50$ and $\tau_0 = 300$. (*a*) Azimuthal velocity profiles. (*b*) Axial velocity profiles.

different values of Re_o and Re_z. Figure 5 shows the velocity profiles with different cylinder radius ratio ε. The gap between the cylinders reduces as ε increases. When ε tends to 1.0, the distributions of the velocity approach those of plane Couette flow and there is no longer an unyielded region in the gap.

3. Linear stability analysis

In the preceding section, the basic flow has been obtained. Considering an infinitesimal disturbance to the basic flow, $\boldsymbol{u}$ and p can be decomposed as $\boldsymbol{u} = \bar{\boldsymbol{u}} + \boldsymbol{u}'$, $p = \bar{p} + p'$, where $\boldsymbol{u}'$ and p' are assumed to vary periodically along the azimuthal and axial directions. The expressions can be written as

$$\boldsymbol{u}' = \boldsymbol{U}(r)\exp(\mathrm{i}(\alpha\theta + \beta z + \kappa t)), \tag{3.1a}$$

$$p' = P(r)\exp(\mathrm{i}(\alpha\theta + \beta z + \kappa t)), \tag{3.1b}$$

where $\boldsymbol{U} = (U_r, U_\theta, U_z)$ and P can be assumed to be a function of r. The linearized disturbance equations are derived by substitution of (3.1*a*), (3.1*b*) into (2.1), (2.2) and subtraction of the basic flow equations. The expressions are

$$\nabla \cdot \boldsymbol{u}' = 0, \tag{3.2}$$

$$\partial_t \boldsymbol{u}' + (\bar{\boldsymbol{u}} \cdot \nabla)\boldsymbol{u}' + (\boldsymbol{u}' \cdot \nabla)\bar{\boldsymbol{u}} = -\nabla p' + \nabla \cdot \tau'. \tag{3.3}$$

The linearized boundary conditions are

$$\boldsymbol{u}'(R_i) = 0, \tag{3.4}$$

$$\boldsymbol{u}'(R_o) = 0. \tag{3.5}$$

If the yield surface does fall in the gap between the cylinders, (3.5) should be replaced by the linearized yield surface boundary conditions ($r = R_y$) (the details are given in Appendix A)

$$\frac{\partial u_r'(R_y)}{\partial r} = 0, \tag{3.6a}$$

$$\frac{\partial u_\theta'(R_y)}{R_y \partial \theta} + \frac{u_r'(R_y)}{R_y} = 0, \tag{3.6b}$$

$$\frac{\partial u_z'(R_y)}{\partial z} = 0, \tag{3.6c}$$

$$\frac{\partial u_\theta'(R_y)}{\partial z} + \frac{\partial u_z'(R_y)}{R_y \partial \theta} = 0, \tag{3.6d}$$

$$\frac{\partial u_\theta'(R_y)}{\partial r} + \frac{\partial u_r'(R_y)}{R_y \partial \theta} - \frac{u_\theta'}{R_y} = -\frac{\partial^2 \bar{u}_\theta(R_y)}{\partial r^2} R', \tag{3.6e}$$

$$\frac{\partial u_r'(R_y)}{\partial z} + \frac{\partial u_z'(R_y)}{\partial r} = -\frac{\partial^2 \bar{u}_z(R_y)}{\partial r^2} R', \tag{3.6f}$$

and the linearized disturbance velocity at the yield surface, i.e.

$$\boldsymbol{u}'(R_y) = 0, \tag{3.7}$$

where R', which describes the initially smooth perturbation of the yield surface. Since the Bingham fluid models a real fluid which behaves both as a viscous fluid and as an elastic solid according to whether or not the yield stress is exceeded, it can be considered that the unyielded regions should be able to maintain an infinitesimal perturbation without breaking up (see Frigaard *et al.* 1994). According to (3.6*a*)–(3.6*f*), the expression of R' can be assumed as

$$R' = \Psi \exp(\mathrm{i}(\alpha\theta + \beta z + \kappa t)), \tag{3.8}$$

where Ψ is the amplitude of the perturbation. Linearizing the nonlinear constitutive equation (2.6), we have

$$\tau = \bar{\tau} + \tau', \tag{3.9}$$

where τ' is the perturbation of τ due to the disturbance of velocity. The components of τ' can be expressed as

$$\tau_{rr}' = \eta \dot{\gamma}_{rr}', \quad \tau_{\theta\theta}' = \eta \dot{\gamma}_{\theta\theta}', \quad \tau_{zz}' = \eta \dot{\gamma}_{zz}', \quad \tau_{z\theta}' = \eta \dot{\gamma}_{z\theta}', \tag{3.10a}$$

$$\tau_{r\theta}' = \eta \dot{\gamma}_{r\theta}' - \chi(\bar{\dot{\gamma}}_{r\theta}, \bar{\dot{\gamma}}_{r\theta})\dot{\gamma}_{r\theta}' - \chi(\bar{\dot{\gamma}}_{r\theta}, \bar{\dot{\gamma}}_{rz})\dot{\gamma}_{rz}', \tag{3.10b}$$

$$\tau_{rz}' = \eta \dot{\gamma}_{rz}' - \chi(\bar{\dot{\gamma}}_{r\theta}, \bar{\dot{\gamma}}_{rz})\dot{\gamma}_{r\theta}' - \chi(\bar{\dot{\gamma}}_{rz}, \bar{\dot{\gamma}}_{rz})\dot{\gamma}_{rz}', \tag{3.10c}$$

where $\eta = (1 + \tau_0/\bar{\dot{\gamma}})$ and $\bar{\dot{\gamma}} = \sqrt{\bar{\dot{\gamma}}_{r\theta}^2 + \bar{\dot{\gamma}}_{rz}^2}$, the definition of function $\chi(x, y)$ is $\chi(x, y) = \tau_0 xy/\bar{\dot{\gamma}}^3$. The terms $\bar{\dot{\gamma}}_{r\theta}$ and $\bar{\dot{\gamma}}_{rz}$ are shearing strain rates of the basic flow. Derivation of these equations is described in detail in Appendix B.

In order to solve the above system numerically, the spatial discretization of (3.3) is achieved by projecting it onto a suitable basis of a velocity space in which (3.2) is satisfied by implication. The definition of the velocity space is

$$\boldsymbol{\Gamma} = \{\boldsymbol{U} \in \Pi(R_i, R_y)^3 | \nabla \cdot \boldsymbol{U} = 0, \boldsymbol{U}(R_i) = \boldsymbol{U}(R_y) = 0\}. \tag{3.11}$$

If all the Bingham fluid in the flow field has been yielded, R_y should be replaced by R_o in the equations above. $\Pi(R_i, R_y)^3$ is the Hilbert space of square-integrable vectorial-functions defined in the interval (R_i, R_y). The definition of the linner product is

$$\langle \boldsymbol{U}, \boldsymbol{V} \rangle = \int_{R_i}^{R_y} \boldsymbol{U}^* \cdot \boldsymbol{V} r \, \mathrm{d}\boldsymbol{r}, \tag{3.12}$$

where * denotes the complex conjugate. For any $\boldsymbol{U} \in \boldsymbol{\Gamma}$ and any pressure function P, it is obvious that $\langle \boldsymbol{U}, \nabla p \rangle = 0$. Therefore, $\boldsymbol{U}$ can be expanded in a suitable basis of $\boldsymbol{\Gamma}$ as

$$\boldsymbol{U} = \sum_n a_n \boldsymbol{U}_n. \tag{3.13}$$

Substituting (3.13), (3.1a) into (3.2) and (3.3), the continuity equation (3.2) is satisfied automatically. Projecting the linearized equations (3.3) onto $\boldsymbol{\Gamma}$, the pressure term disappears and we obtain a linear system for the coefficient a_n

$$\lambda \sum_n \langle \tilde{\boldsymbol{U}}_m, \boldsymbol{U}_n \rangle a_n = \sum_n \langle \tilde{\boldsymbol{U}}_m, (\boldsymbol{U}_n \cdot \nabla \bar{\boldsymbol{u}} + \bar{\boldsymbol{u}} \cdot \nabla \boldsymbol{U}_n - \nabla \cdot \tau'(\bar{\boldsymbol{u}}, \boldsymbol{U}_n)) \rangle a_n, \tag{3.14}$$

where $\lambda = -\mathrm{i}\kappa$, $\tau'(\bar{\boldsymbol{u}}, \boldsymbol{U}_n)$ can be determined by equations (3.10a)–(3.10c).

The Galerkin scheme is implemented, where the basis ($\{\boldsymbol{U}_n\}$) used to expand the velocity is the same to that used for projection ($\{\tilde{\boldsymbol{U}}_m\}$). A detailed discussion may be found in Moser, Moin & Leonard (1983), Canuto *et al.* (1988) or Meseguer & Marques (2000). According to the definition of velocity space in (3.11), a basis for $\boldsymbol{\Gamma}$ can be chosen as

$$\boldsymbol{U}_j^1 = (0, -r\beta\phi_j, \alpha\phi_j), \tag{3.15}$$

$$\boldsymbol{U}_j^2 = (-\mathrm{i}\beta\psi_j, 0, \mathrm{D}_+\psi_j), \tag{3.16}$$

where $\mathrm{D} = \partial_r$, $\mathrm{D}_+ = \partial_r + 1/r$. The terms ϕ_j and ψ_j are functions satisfying the boundary conditions $\phi_j = \psi_j = \mathrm{D}\psi_j = 0$ on R_i and R_y. From (3.6a)–(3.6f) we have

$$\sum_j -a_j^1 R_y \beta \mathrm{D}\phi_j + \mathrm{D}^2 \bar{u}_\theta(R_y)\Psi = 0, \tag{3.17}$$

$$\sum_j \left(a_j^1 \alpha \mathrm{D}\phi_j + a_j^2 \mathrm{D}\,\mathrm{D}_+\psi_j\right) + \mathrm{D}^2 \bar{u}_z(R_y)\Psi = 0, \tag{3.18}$$

where a_j^1 and a_j^2 are coefficients in (3.13). It must be pointed out that if all the Bingham fluid in the gap has been yielded, the yield surface does not appear and equations (3.17) and (3.18) should be ignored. Introduce the new radial coordinate

$$x = 2\left(\frac{r - R_i}{R_y - R_i}\right) - 1, \tag{3.19}$$

N	Re_{ic}	β_c
8	192.9022 9534	3.9427 5222
16	192.9053 4161	3.9423 8312
24	192.9053 4160	3.9423 2700
32	192.9053 4160	3.9423 2544
40	192.9053 4160	3.9423 2175
48	192.9053 4160	3.9423 2685

TABLE 1. Critical values with different spectral approximate order, when $\varepsilon = 0.5$, $Re_o = 30$, $Re_z = 30$ and $\tau_o = 300$, $\alpha = -1$ being the dominant azimuthal mode. The position of the yield surface is $R_y = 1.86$.

where $x \in [-1, 1]$ and R_y should be replaced by R_o if all the Bingham fluid has been yielded. A simple choice for ϕ_j and ψ_j, which satisfies the boundary conditions (3.4) and (3.7), is

$$\phi_j(r) = (1 - x^2)T_j(x), \quad \psi_j(r) = (1 - x^2)^2 T_j(x), \tag{3.20}$$

where $T_j(x)$ is the Chebyshev polynomials. With this choice, all inner products in (3.14) can be numerically computed through Gauss–Legendre quadrature. Finally, the generalized complex eigenvalue system of (3.14) can be written as

$$\boldsymbol{H}\boldsymbol{x} = \lambda \boldsymbol{G}\boldsymbol{x}, \tag{3.21}$$

where $\lambda = -\mathrm{i}\kappa$ and the vector $\boldsymbol{x}$ contains the real and imaginary parts of the coefficients a_n defined in (3.13). $\boldsymbol{H}$, $\boldsymbol{G}$ are constant matrices dependent on the basic flow and $\boldsymbol{G}$ is positive definite.

For numerical computation, normally, it is necessary to choose $j = 0, 1, 2, \ldots, N-1$. Including all a_j^1, a_j^2 and Ψ, there are $2N+1$ unknowns; however, combining (3.17), (3.18) and (3.21), $2N+2$ equations are obtained. It is clear that the problem is caused by the finite truncation of the series in (3.13). The methods used to resolve the problem are similar to those used by Orszag (1971), whereby the eigenvalue problem of (3.21) can be written in the explicit functional form

$$\lambda = \lambda(Re_i, Re_o, Re_z, \tau_0, \varepsilon, \beta, \alpha). \tag{3.22}$$

It should be remarked that (3.22) is a function of the parameters which have dominating effects on the dynamic characteristics of the system. The resulting algebraic generalized eigenvalue problem is solved with a public-domain subroutine which uses QZ factorization (Garbow 1978). For given Re_o, Re_z, τ_0, ε and α, the curves of $Re(\lambda) = 0$ in the (β, Re_i)-plane are termed neutral stability curves (NSC). As will be seen in the following section, the NSC curves for the problem may have multiple extrema (maxima and minima), and exhibit disconnected parts and sharp geometrical forms. The critical parameters (Re_{ic}, β_c), which are the local extremum values of NSC, are calculated with different parameters. The convergence of the numerical method is shown in table 1, where the critical inner Reynolds number Re_{ic} and the critical axial wavenumber β_c are presented as a function of the number of spectral modes (N) considered for the calculation in each case. It shows that $N = 24$ is sufficient for the computation of linear stability here.

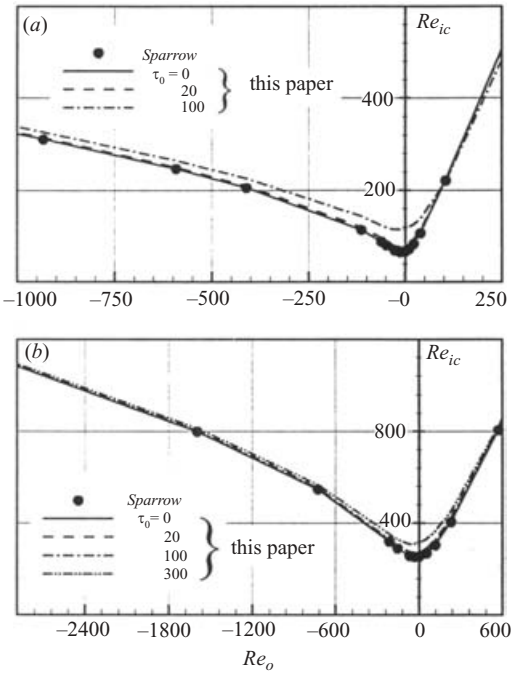

FIGURE 6. Comparison between the results of Sparrow *et al.* (1964) and those in this paper. (*a*) $\varepsilon = 0.5$. (*b*) $\varepsilon = 0.75$.

4. Results and discussions

In this section, the stabilizing effects of $Re_o, Re_z, \tau_0, \varepsilon$ are studied. The Taylor–Couette flow ($Re_z = 0$) of Bingham fluid is considered in the first part of this section in order to provide a basis for the main results of this work. The effects of yield stress on the flow instability are the main concern. In the second part, the axial sliding flow with rigid rotation is studied. In the last part, the more complex spiral Couette flow is studied and some new phenomena, related to the yield stress, are presented in detail.

4.1. *Taylor–Couette flow*

The instability of the Taylor–Couette problem is studied first in the absence of axial flow in order to check the feasibility of the computational method and the validity of the code in this study. The axisymmetric disturbances are involved because of the axisymmetric basic flow. First of all, we solved the stability problem in hand for the Newtonian fluid case ($\tau_0 = 0.0$). For comparison with earlier results obtained by Sparrow *et al.* (1964), the neutral stability curves (NSC) of Taylor–Couette flow are presented. This shows that our results fully coincide with the previous computations (see figure 6). The yield stress has a distinct stabilizing effect on the flow when Re_o tends to 0. In the counter-rotating state, the stabilizing effects are more effective at low Re_o values than high. These results are expected according to the constitutive equation (2.6). It shows that at large shearing strain, the yield stress makes little contribution to the effective viscosity η and the dynamic characteristics of Bingham fluid approximate those of Newtonian fluid. From the comparison between figures 6(*a*) and 6(*b*), it can be seen that with the same value of τ_0, Re_o, the value of Re_{ic} for $\varepsilon = 0.75$ is much greater than that for $\varepsilon = 0.5$. The explanation is that with the increasing value of radius ratio ε, the gap between cylinders decreases and the

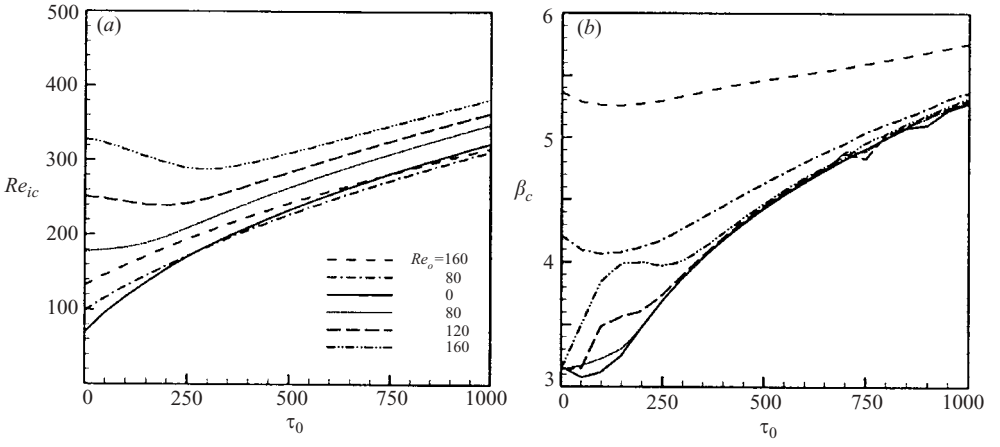

FIGURE 7. Critical parameters as a function of τ_0, under different Reynolds number Re_o with $\varepsilon = 0.5$. (*a*) Critical Reynolds number Re_{ic}. (*b*) Critical axial wavenumber β_c.

distributions of the velocity approach those of plane Couette flow, so that the flow becomes stable.

From (2.6), the effective viscosity η increases with increasing yield stress. Figure 7 shows Re_{ic} and β_c as a function of τ_0 with different values of Re_o. In the counter-rotating state (where $Re_o < 0$), it can be seen that the stabilizing effects of the yield stress on the fluid instability are dominant. The critical Reynolds number Re_{ic} increases monotonically with increasing τ_0 (see figure 7*a*). In the co-rotating state (where $Re_o > 0$), for $Re_o = 80$ the critical Reynolds number Re_{ic} also increases monotonically with increasing τ_0. However, if we move to a higher Re_o value ($Re_o = 120, 160$), the critical Reynolds number Re_{ic} decreases with increasing τ_0 while τ_0 falls in the low-value region. This phenomenon can also be seen in figure 6(*a*), in which the curve of Bingham fluid falls below that of Newtonian fluid as the outer Reynolds number Re_o moves to a high value. This is because when Re_o is large, the viscosity plays a minor role in the flow instability. From § 2, it is known that, owing to the effects of the yield stress, the velocity profiles can be made steeper than the profiles of the Newtonian flow, so that the flow can be made unstable.

To give a physical explanation of the role of the yield stress, the energy of the disturbance flow is considered, which in association with (3.3) is readily found to be

$$\frac{\mathrm{d}E'}{\mathrm{d}t} = S + S_1 - \Phi, \tag{4.1}$$

where

$$E' = \oint_V \tfrac{1}{2}\left(u_r'^2 + u_\theta'^2 + u_z'^2\right) \mathrm{d}V, \tag{4.2}$$

$$S = -\oint_V \left(\mathrm{D}\bar{u}_\theta - \frac{\bar{u}_\theta}{r}\right) u_r' u_\theta' \, \mathrm{d}V, \tag{4.3}$$

$$S_1 = \oint_V \chi(\bar{\dot{\gamma}}_{r\theta}, \bar{\dot{\gamma}}_{r\theta})(\dot{\gamma}'_{r\theta})^2 \, \mathrm{d}V, \tag{4.4}$$

$$\Phi = \oint_V \tfrac{1}{2}\eta[(\dot{\gamma}'_{rr})^2 + (\dot{\gamma}'_{\theta\theta})^2 + (\dot{\gamma}'_{zz})^2 + 2(\dot{\gamma}'_{r\theta})^2 + 2(\dot{\gamma}'_{\theta z})^2 + 2(\dot{\gamma}'_{rz})^2] \, \mathrm{d}V. \tag{4.5}$$

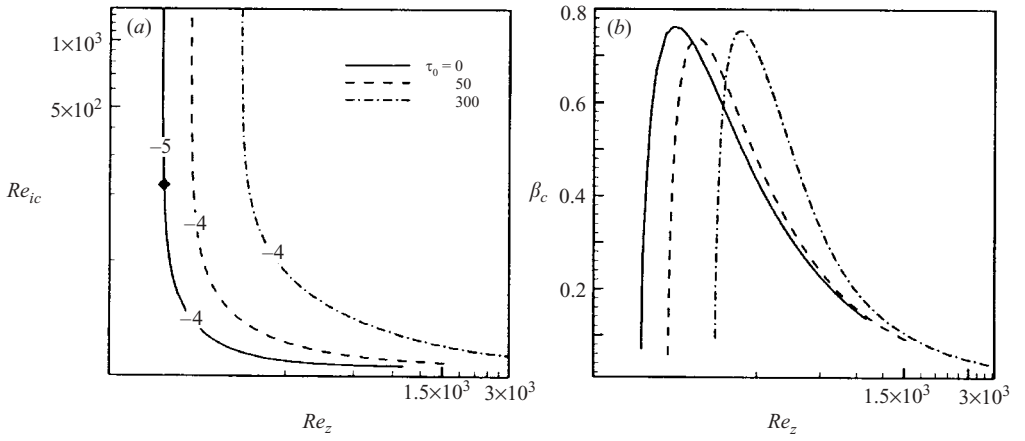

FIGURE 8. Sliding rigid rotation with different value of τ_0. (*a*) Critical Reynolds number Re_{ic} and (*b*) critical wavenumber β_c as a function of the axial Reynolds number Re_z.

The integration in each case is performed over a disturbance cell. Since in § 2, it has been indicate that the velocity profiles become steep along the gap with increasing yield stress, S can be influenced by the yield stress indirectly. On the other hand, Φ, the dissipation function associated with the disturbance, is also increased owing to the increasing yield stress. This means that the fluid is now better able to dissipate the disturbance energy. S_1, which is positive definite, is a very large item in comparison with the energy equation in Graebel (1962). It can be understood that S_1 is caused by variation of the effective viscosity due to the effects of the disturbance. Clearly, S_1 can cause the transfer of energy from the basic flow to the disturbance flow, which can make the flow unstable. For the neutrally stable case $\mathrm{d}E'/\mathrm{d}t = 0$, then, the value of $S + S_1$ must be greater than Φ to cause instability.

In § 2, when τ_0 is large enough, an unyielded region will be generated in the gap. Although it seems that the distrubance of the yield surface can be regarded as a destabilizing agent, from figure 7, according to the fairly smooth curves, the presence of a yield surface plays no role in the stabilizing criterion. This result is perhaps because the yield surface is an interior surface instead of a material surface. The disturbance waves on the surface are not able to redistribute effectively the energy involved. In figure 7(*a*), when τ_0 is large, either in a co-rotating or a counter-rotating state, the critical Reynolds number Re_{ic} increases almost linearly with increasing τ_0. The critical axial wavenumbers, as a function of τ_0, are shown in figure 7(*b*). When τ_0 is large enough, the critical axial wavenumbers β_c are approximately independent of Re_o in the co-rotating state. These can be understood according to the increase of the unyielded region with increasing τ_0, which can make the flowing (yielded) region smaller and cause the flow to be stable.

4.2. *Axial sliding with rigid rotation* ($Re_i = \varepsilon Re_o$)

In this section, we analyse the rigid rotation case $\Omega_i^* = \Omega_o^*$ (or $Re_i = \varepsilon Re_o$) with sliding of the inner cylinder along the axial direction. This is relevant to understanding the effects of the yield stress on the shearing instability mechanism. In § 2, when $Re_z = 0$, all Bingham fluid in the gap between the cylinders remains unyielded because of the existence of the yield stress. So stabilization is constanty maintained.

Figure 8 shows the computed critical Reynolds number $Re_{ic} = \varepsilon Re_o$ and critical wavenumber β_c as a function of the axial speed Re_z with different τ_0. The logarithmic

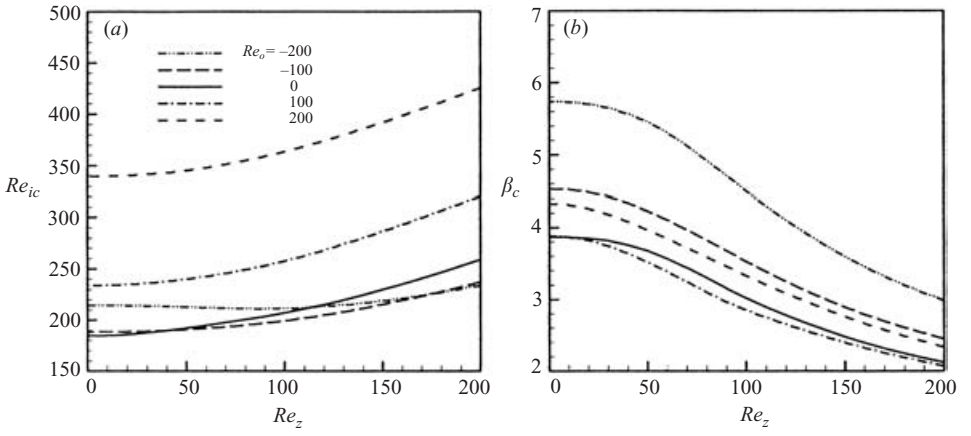

FIGURE 9. Critical parameters as a function of Re_z with various Re_o, while $\tau_0 = 300$, $\varepsilon = 0.5$ and $\alpha = 0$. (*a*) Critical Reynolds number Re_{ic}. (*b*) Critical axial wavenumber β_c.

coordinates are used. The critical regime has an asymptotic value as Re_z is increased. The dependence of the critical wavenumber β_c on the neutral curve is depicted in figure 8(*b*). The presence of a maximum can be observed and the value of β_c decreases as the axial Reynolds number Re_z increases. Similar results can be found in Meseguer & Marques (2000).

Nevertheless, as has been mentioned above, for large shearing strain, the yield stress makes little contribution to the effective viscosity η and the dynamic characteristics of Bingham fluid approximate those of Newtonian fluid. It can be seen in figure 8(*a*) that the yield stress has distinct stabilizing effects while Re_z is small. For τ_0 increasing from 0 to 300, the asymptotic value of Re_z, as Re_{ic} is increased, varies from 85.11 to 190.24. In this limit, the critical azimuthal wavenumber varies from $\alpha = -5$ ($\tau_0 = 0$) to $\alpha = -4$ ($\tau_0 = 300$). In figure 8(*b*), the value of Re_z, for which the maximum of β_c occurs, varies from 122.05 to 249.95. On the other hand, as the axial sliding Reynolds number increases, the critical rotation Reynolds number Re_{ic} approaches a uniform asymptotic value 33.24, which is independent of the yield stress. In figure 8(*b*), the critical wavenumber also approaches the value for Newtonian flow with increasing Re_z.

4.3. *Spiral Couette flow*

In § 4.1, Taylor–Couette flow of Bingham fluid has been studied, in which $Re_z = 0$ is required and only the axisymmetric disturbances are considered. In this section, the effects of axial sliding are included and both the axisymmetric and non-axisymmetrical disturbances are considered. The dominant azimuthal modes of disturbances are computed at different values of Re_o, Re_z and τ_0.

First, the effects of Re_o, Re_z and τ_0 on the flow instability with axisymmetric disturbances are studied. From § 4.1, it is indicated that the rotation of the outer cylinder generally has a stabilizing effect on the Taylor–Couette flow and the co-rotating state is more stable than the counter-rotating state. The same results can also be found in the spiral-Couette flow, where there is axial sliding of the inner cylinder. Figure 9(*a*) shows Re_{ic} as a function of Re_z with different Re_o. It shows that Re_{ic} is increased owing to the increasing of Re_z. This is because, with the existence of the axial sliding, monodirectional vorticities can be generated from the sliding wall of the inner cylinder and transferred into the flow field due to the effects of viscosity. So the axial sliding

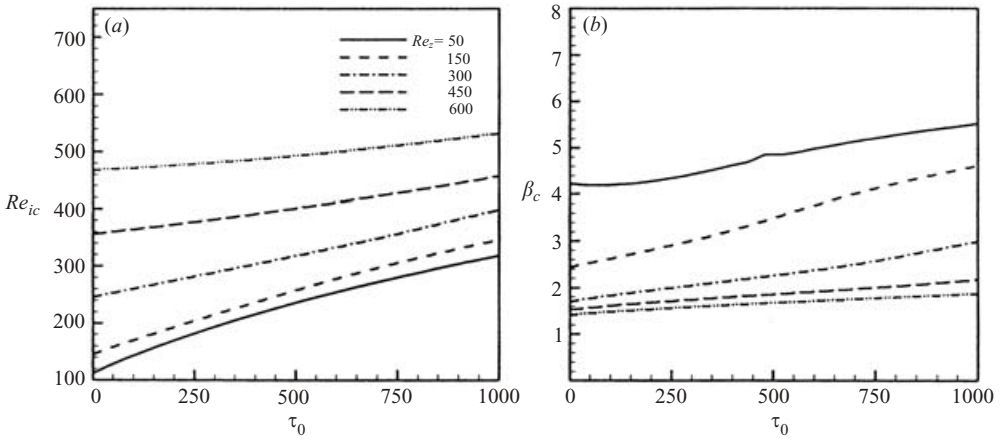

FIGURE 10. Critical parameters as a function of τ_0, with different Re_z while $\varepsilon = 0.5$, $\alpha = 0$ and $Re_o = -120$. (*a*) Critical Reynolds number Re_{ic}. (*b*) Critical axial wavenumber β_c.

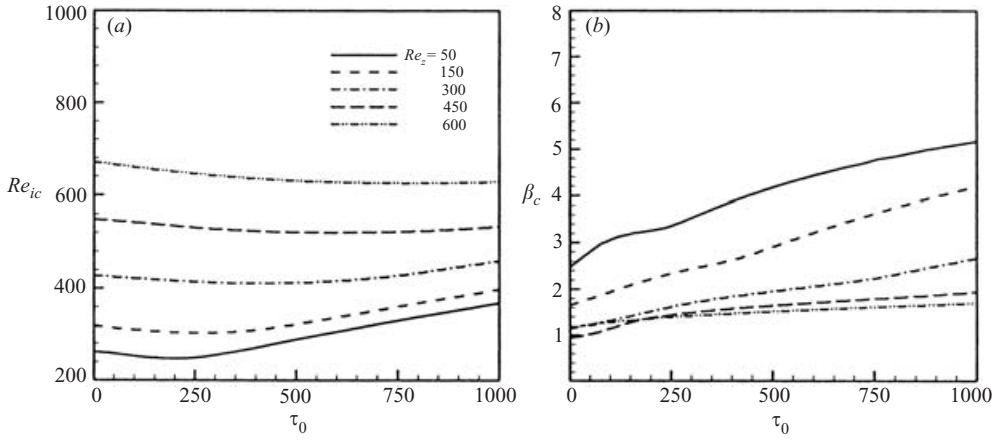

FIGURE 11. Critical parameters as a function of τ_0, with different Re_z while $\varepsilon = 0.5$, $\alpha = 0$ and $Re_o = 120$. (*a*) Critical Reynolds number Re_{ic}. (*b*) Critical axial wavenumber β_c.

movement has some stabilizing effects on the spiral-Couette flow with axisymmetric disturbances mode. From figure 9(*a*), we can see that the stabilizing effects of the sliding on the axisymmetric disturbance mode ($\alpha = 0$) are mainly in the co-rotating case. These effects are also reported by Ali & Weidman (1993) and Meseguer & Marques (2000) for the same Newtonian fluid flow. Figure 9(*b*) shows that the value of the critical axial wavenumber β_c descends monotonically with increasing Re_z.

Figures 10 and 11 show the curves of Re_{ic} and β_c as a function of τ_0 with different Re_z in the counter-rotating state ($Re_o = -120$) and co-rotating state ($Re_o = 120$). The stabilizing effects of the axial sliding movement are also shown here. From § 4.1, it is known that τ_0 has a general stabilizing effect on the flow with $Re_z = 0$ in the counter-rotating state. This can also be seen in figure 10(*a*). From § 2, the axial velocity $\bar{u}_z$ and the azimuthal velocity $\bar{u}_\theta$ are interdependent because of the existence of the yield stress. When Re_z is large, the yield stress makes little contribution to the effective viscosity η. So the effects of the yield stress on the dynamic characteristics of Bingham fluids are weak for the flow with large Re_z and small τ_0. It can be seen in figure 10(*a*)

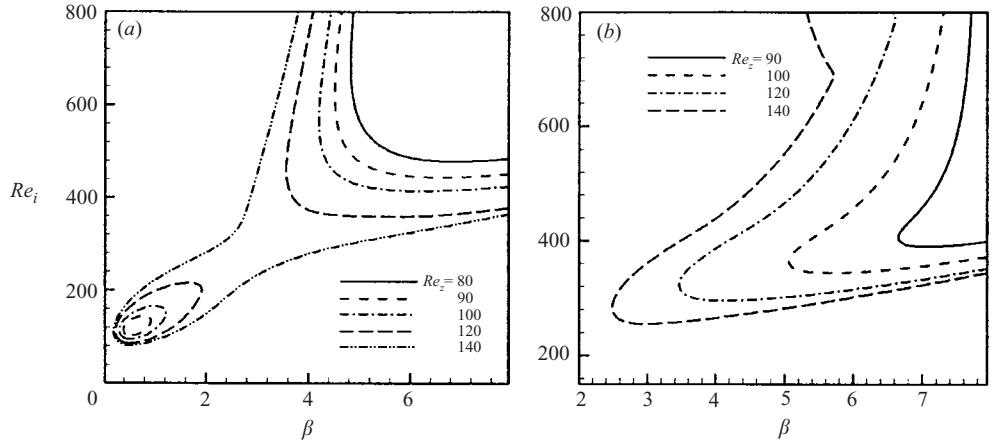

FIGURE 12. Neutral stability curves for spiral Couette flow at different Re_z, while $Re_o = 200$, $\varepsilon = 0.5$, $\alpha = -4$. (*a*) $\tau_0 = 0$, curves for Newtonian fluid. (*b*) $\tau_0 = 300$, curves for Bingham fluid.

that the stabilizing effects of τ_0 are stronger with a low value of Re_z than those with a high value of Re_z. The critical axial wavenumber β_c is nearly independent of τ_0 when Re_z is a high value. This can be seen in figures 10(*b*) and 11(*b*). In figure 11(*a*), for the co-rotating state, a descending section of Re_{ic} can be found with increasing τ_0, just like those in figure 7(*a*). The value of τ_0, at which the minimum of Re_{ic} appears, increases with increasing Re_z.

Up to now, only the axisymmetric disturbances ($\alpha = 0$) have been considered. Since perturbations, which can be decomposed into different azimuthal modes, are generated owing to the non-uniform or oscillating flow field, the non-axisymmetrical disturbances ($\alpha \neq 0$) obviously do exist and should be considered carefully. The results are distinctly different from those with axisymmetric disturbances ($\alpha = 0$). Figure 12 shows the neutral stability curves of the Newtonian and Bingham fluids for $Re_o = 200$, $\varepsilon = 0.5$, $\alpha = -4$. For Newtonial fluid, the island of instability appears for $Re_z = 82.64$ figure 12(*a*). Owing to the appearance of the island, we have three extrema for Re_i, two minima and a maximum. The neutral stability curve has two disconnected branches. The absolute minimum of Re_i (termed the critical Reynolds number Re_{ic}) becomes discontinuous (zeroth-order discontinuity) as soon as the island of instability appears (figure 13, solid lines). Meseguer & Marques (2000) have discussed this phenomenon, particularly in the Newtonian flow, and pointed out that the competition between centrifugal and shear instability causes the neutral stability curves to develop islands of instability. Similar islands of instability have also been found in Mcfadden *et al.* (1990) and Marques & Lopez (1997). Figure 12(*b*) shows the neutral stability curve of Bingham fluid with the Hedstrom number $\tau_0 = 300$. It can be seen that the islands of instability cannot be developed again and the discontinuity disappears. Plotting the position of all the absolute minimal values of Re_i as a function of Re_z with $Re_o = 200$ and different τ_0, the solid curves shown in figure 13 are obtained, where the dashed curves correspond to the other extrema. The numbers marked on the curves are the critical azimuthal mode α. The curves appears to have discontinuities in the derivative (first-order discontinuities), when the critical azimuthal mode changes. The figure shows that the critical Reynolds number Re_{ic} is discontinuous (zeroth-order discontinuity) for small values is of τ_0. When $\tau_0 = 0$, the Bingham fluid can be treated as a Newtonian fluid and the results are

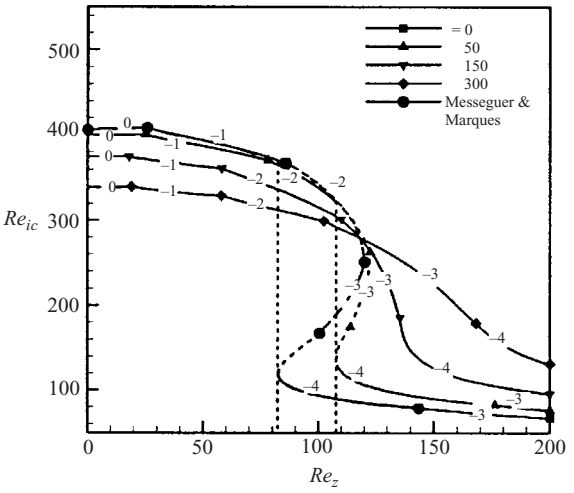

FIGURE 13. The critical inner Reynolds number Re_{ic} as a function of Re_z under different τ_0, when $Re_o = 200$, $\varepsilon = 0.5$.

consistent with those of Meseguer & Marques (2000). The discontinuity appears for $Re_z = 82.64$ (consistent with Meseguer & Marques 2000). When $\tau_0 = 50$, the position of the discontinuity moves to $Re_z = 107.72$. When $\tau_0 = 150$, it can be seen that the discontinuity nearly disappears. This means that the yield stress can have effects that inhibit the generation of discontinuity. When τ_0 is large enough, such as $\tau_0 = 300$, for our calculation, no discontinuity can be generated. The discontinuity of the critical parameter depends on the experimental conditions. If Re_o is fixed and $Re_{ic}(\tau_0, Re_o, Re_z)$ calculated, the zeroth-order discontinuity would be found, as shown in figure 13. However, if Re_o is fixed and $Re_{zc}(\tau_0, Re_i, Re_o)$ calculated, a continuous result is found. We have followed the latter conditions to obtain the critical surface in the fold region. Figure 14 show perspective views of the critical surface with $\tau_0 = 50$ and 300. When $\tau_0 = 50$, the whole critical surface is multivalued and continuous, but a fold is developed (figure 14*a*). However, when $\tau_0 = 300$, the critical surface is single-valued. Compared with a similar surface of Newtonian fluid (Meseguer & Marques 2000), it is clear that with the existence of the yield stress, the fold region is attenuated. Being similar to those in § 4.1, the energy equation of the disturbance flow can also be written as (4.1) except that S and S_1 are

$$S = -\oint_V \left[u'_r u'_\theta \left(\mathrm{D}\bar{u}_\theta - \frac{\bar{u}_\theta}{r} \right) + u'_r u'_z \mathrm{D}\bar{u}_z \right] \mathrm{d}V, \tag{4.6}$$

$$\begin{aligned} S_1 &= \oint_V [\chi(\bar{\dot{\gamma}}_{r\theta}, \bar{\dot{\gamma}}_{r\theta})(\dot{\gamma}'_{r\theta})^2 + 2\chi(\bar{\dot{\gamma}}_{r\theta}, \bar{\dot{\gamma}}_{rz})\dot{\gamma}'_{r\theta}\dot{\gamma}'_{rz} + \chi(\bar{\dot{\gamma}}_{rz}, \bar{\dot{\gamma}}_{rz})(\dot{\gamma}'_{rz})^2] \, \mathrm{d}V \\ &= \oint_V \frac{\tau_0}{\bar{\dot{\gamma}}^3} (\bar{\dot{\gamma}}_{r\theta}\dot{\gamma}'_{r\theta} + \bar{\dot{\gamma}}_{rz}\dot{\gamma}'_{rz})^2. \end{aligned} \tag{4.7}$$

S_1, which is positive definite, can cause the flow to be unstable. Although, in § 2, the velocity components $(\bar{u}_\theta, \bar{u}_z)$ of the basic flow depend upon each other because of the existence of yield stress, in (4.6), it seems that S is just the linear combination of the terms caused by Taylor–Couette flow and axial sliding. However, in (4.7), the combination is nonlinear when $\tau_0 > 0$. This indicates that the instabilities caused by rotating and axial sliding are related owing to the effects of yield stress.

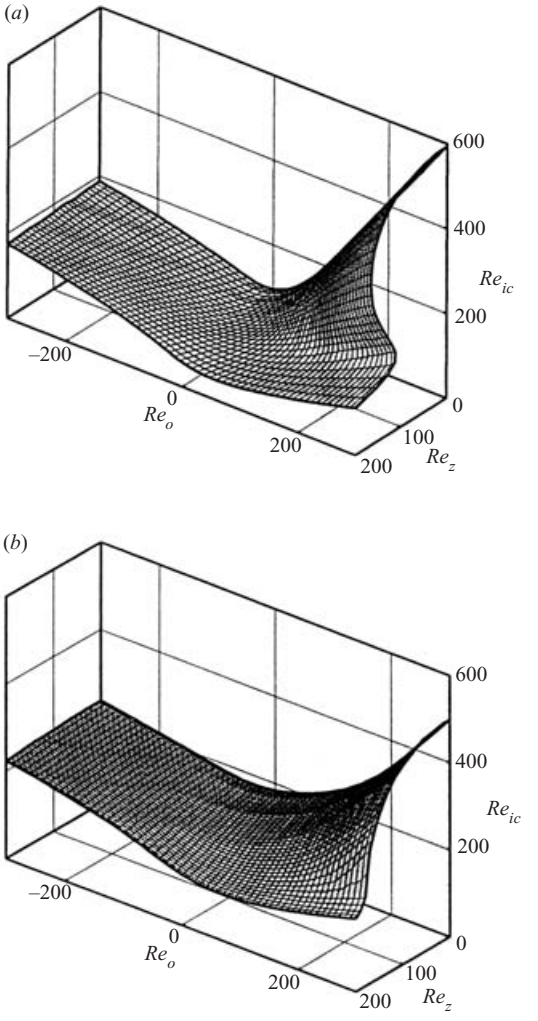

FIGURE 14. Perspective view of the critical surface $Re_{ic}(\tau_0, Re_o, Re_z)$ for $\varepsilon = 0.5$. (*a*) $\tau_0 = 50$. (*b*) $\tau_0 = 300$.

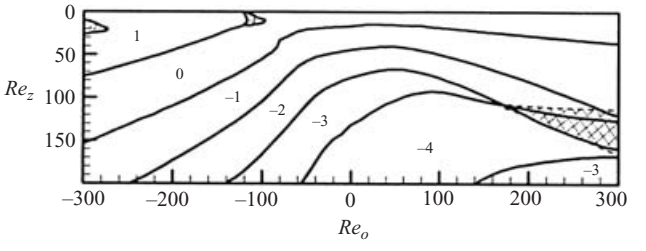

FIGURE 15. Dominant azimuthal mode α criticality at various Re_o and Re_z, while $\tau_0 = 50$ and $\varepsilon = 0.5$. The shaded region corresponds to the fold, whose edges are plotted as dashed lines.

Figure 15 is the projection of the critical surface $Re_{ic}(\tau_0, Re_o, Re_z)$ onto the (Re_o, Re_z) surface when $\tau_0 = 50$. The curves corresponding to the change in the azimuthal mode α are plotted. This shows the most unstable azimuthal mode of the disturbance

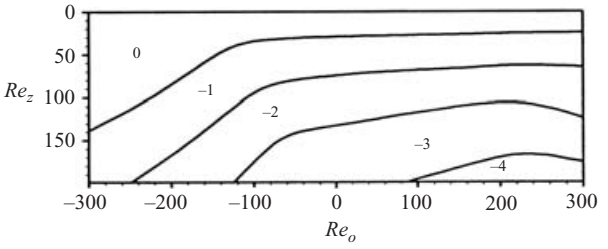

FIGURE 16. Dominant azimuthal mode α criticality at various Re_o and Re_z, while $\tau_0 = 300$ and $\varepsilon = 0.5$.

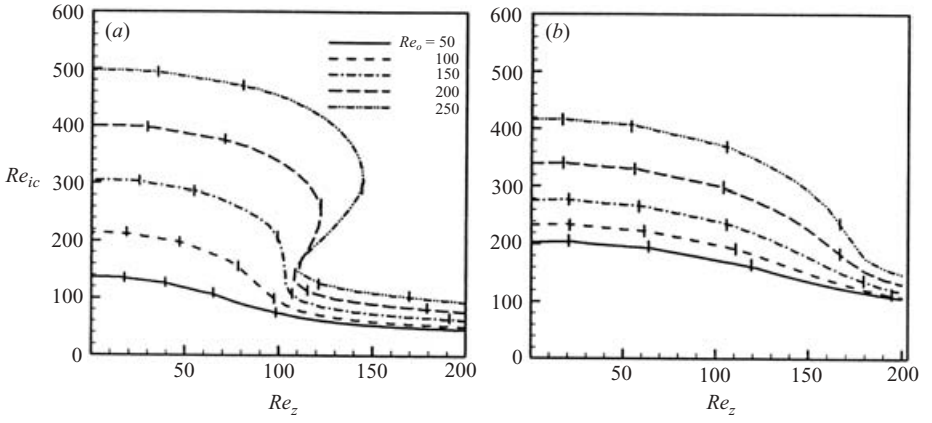

FIGURE 17. The critical inner Reynolds number Re_{ic} as a function of Re_z in the co-rotating state while $\varepsilon = 0.5$. (*a*) $\tau_0 = 50$. (*b*) $\tau = 300$.

for particular, Re_o and Re_z. It can be seen that, along these curves, the change in α is always ± 1, except close to the $Re_z = 0$ axis and near the shaded region. The same phenomena are found in the flow of Newtonian fluids. Meseguer & Marques (2000) explained these by introducing the competition between $\pm\alpha$ modes (when $Re_z \sim 0$) or the competition between the centrifugal instability and the shear instability. Figure 16 is the projection of surface $Re_{ic}(\tau_0, Re_o, Re_z)$ onto the (Re_o, Re_z) surface when $\tau_0 = 300$. The changes in α are always ± 1. Comparing figures 15 and 16, it can be seen that when Re_z is small enough ($Re_z \sim 0$), for the co-rotating states, the most unstable disturbance, which is about to be amplified and leads to the destabilization of the flow, is the axisymmetric ($\alpha = 0$) azimuthal mode. The yield stress can effectively inhibit the competition between the two instability mechanisms and the competition between mode $\pm\alpha$ when $Re_z \sim 0$.

Figure 17 shows Re_{ic} as a function of Re_z for different values of Re_o in the co-rotating state when $\tau_0 = 50$ and $\tau_0 = 300$. The points where the azimuthal wavenumber α changes, are distinguished by vertical bars. In figure 17(*a*), for $\tau_0 = 50$, sections of the bulge region are displayed. The Re_{ic} grows dramatically with increasing Re_o in the region with low values of Re_z, which suggests that the centrifugal instability is the dominant instability mechanism. However, with increasing Re_z, the effects of shear instability are intensified, especially for disturbance with a non-axisymmetric mode. The discontinuities are generated as a result of the competition between the centrifugal and shear instability mechanisms. However, in figure 17(*b*), for $\tau_0 = 300$, no discontinuity grows while Re_z increases. Comparing figures 17(*a*) and 17(*b*) shows

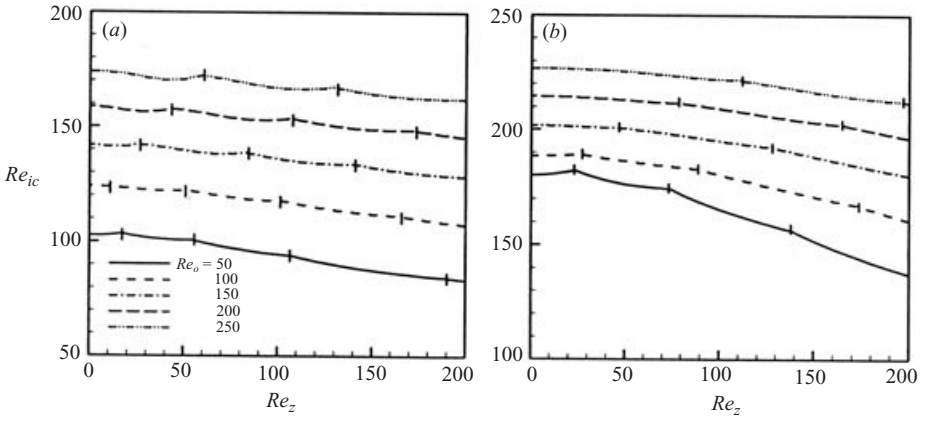

FIGURE 18. The critical inner Reynolds number Re_{ic} as a function of Re_z in the counter-rotating state while $\varepsilon = 0.5$. (*a*) $\tau_0 = 50$. (*b*) $\tau_0 = 300$.

that the yield stress appears to have destabilizing effects on the flow stability in the co-rotating state with large Re_o and small Re_z. Figure 18 shows Re_{ic} as a function of Re_z for different values of Re_o in the counter-rotating state when $\tau_0 = 50$ and $\tau_0 = 300$. Here, Re_{ic} changes smoothly and almost independently of the axial sliding Re_z, which suggests that the centrifugal instability is the dominant instability mechanism, especially for large Re_o. Comparing figures 17 and 18 also indicates that the effect of axial sliding on axisymmetric modes is slightly stabilizing (mainly in the co-rotating state as mentioned before), in contrast to their destabilizing effect on non-axisymmetric modes.

5. Conclusion

In this work, the stability problem for a Bingham-fluid spiral-Couette flow has been considered. The analytic solution of the basic flow has been derived. The effects of axial sliding, outer cylinder rotation and the yield stress on the flow stability have been analysed comprehensively. In the open geometry, the wide gap with radius ratio $\varepsilon = 0.5$ has been studied in detail because the instability appears at lower Reynolds number than in the narrow-gap cases. The code has been checked by comparing with the results of Sparrow *et al.* (1964) and Meseguer & Marques (2000). The Newtonian results have been reproduced when $\tau_0 = 0$.

For the Taylor–Couette flow, we have found that the yield stress does have some destabilizing effects in the co-rotating regime with a relatively large value of Re_o. This is due to the effects of yield stress on the deformation rate of the basic flow, which helps to transfer energy from the unperturbed flow to the perturbation. However, on the other hand, when τ_0 is large enough, the yield stress plays a stabilizing role on the flow instability owing to the presence of the unyielded region, which leads the flow region to be narrowed. As mentioned above, the flow is more stable in the narrow-gap case than in the wide-gap case. The yield surface, which has been treated as a free surface, has no effect on the stability criterion.

For the spiral-Couette flow, the presence of axial flow introduces new stresses into the problem, which potentially change the dominant balances in the momentum equations. When $\tau_0 = 0$, two instability mechanisms, caused by the rotating flow and the axial shearing flow, are independent of each other. We found that the critical

surface $Re_{ic} = Re_{ic}(Re_o, Re_z)$ has multiple values in the co-rotating region. This is due to the presence of a sudden dominant island of instability corresponding to a different azimuthal mode, which can be observed from the neutral stability curves (NSC): This phenomenon can be explained in term of competition between these two instability mechanisms. However, when $\tau_0 > 0$, the velocity components $(\bar{u}_\theta, \bar{u}_z)$ of the basic flow affect each other because of the existence of yield stress. When τ_0 has a large value, the critical surface changes smoothly, and no discontinuities and islands of instability can be found. It appears that the yield stress plays an important role in inhibiting the competition between the centrifugal and shear instability mechanisms.

Important differences can be seen between the co-rotating and counter-rotating regions. The latter configurations exhibit a regular behaviour in the critical regime. Nevertheless, for the Newtonian fluid, we find a sudden dominance of non-consecutive azimuthal modes with low Re_z. This is due to the mode competition and switching between $\pm\alpha$ modes. However, for the Bingham fluid, when τ_0 has a large value, the azimuthal modes change consecutively. This is due to the inhibiting effects of the yield stress on the mode competition and switching. Though there are differences between co-rotating and counter-rotating states, generally the rotation of the outer cylinder does have some stabilizing effects on the flow.

The authors are very grateful for the support of the Natural Science Foundation of China under Grant no. 19834020 and the RFDP under Grant no. 2000000310.

Appendix A. Linearization of boundary conditions at the yield surface

The complete derivation of the linear yield surface boundary condition (3.7), is presented here.

First, $\dot{\boldsymbol{\gamma}}(\boldsymbol{u}(R_y + R')) = 0$ is satisfied at each perturbed yield surface owing to the yield criterion and continuity of stress throughout the flow field. It can be expanded at R_y, i.e.

$$\begin{aligned}\dot{\boldsymbol{\gamma}}(\boldsymbol{u}(R_y + R')) &= \dot{\boldsymbol{\gamma}}(\bar{\boldsymbol{u}}(R_y + R')) + \dot{\boldsymbol{\gamma}}(\boldsymbol{u}'(R_y + R')) \\ &= \dot{\boldsymbol{\gamma}}(\bar{\boldsymbol{u}}(R_y)) + \frac{\partial \dot{\boldsymbol{\gamma}}(\bar{\boldsymbol{u}}(R_y))}{\partial r} R' + \dot{\boldsymbol{\gamma}}(\boldsymbol{u}'(R_y)) + O(R'^2), \end{aligned} \tag{A 1}$$

where $\dot{\boldsymbol{\gamma}}(\bar{\boldsymbol{u}}(R_y)) = 0$ and through linearization, from (A 1) we obtain

$$\dot{\boldsymbol{\gamma}}(\boldsymbol{u}'(R_y)) = -\frac{\partial \dot{\boldsymbol{\gamma}}(\bar{\boldsymbol{u}}(R_y))}{\partial r} R'. \tag{A 2}$$

The conditions (3.6*a*)–(3.6*f*) follow directly from (A 2).

Secondly, the velocity at the yield surface can also be expanded at R_y, i.e.

$$\begin{aligned}\boldsymbol{u}(R_y + R') &= \bar{\boldsymbol{u}}(R_y + R') + \boldsymbol{u}'(R_y + R') \\ &= \bar{\boldsymbol{u}}(R_y) + \frac{\partial \bar{\boldsymbol{u}}(R_y)}{\partial r} R' + \boldsymbol{u}'(R_y) + O(R'2). \end{aligned} \tag{A 3}$$

The components of the velocity at the yield surface are

$$u_r(R_y + R') = 0, \tag{A 4a}$$

$$u_\theta(R_y + R') = \frac{Re_o}{R_o}(R_y + R'), \tag{A 4b}$$

$$u_z(R_y + R') = 0. \tag{A 4c}$$

Through linearization of (A 3) and combination with (A 4*a*)–(A 4*c*), we can derive

$$\boldsymbol{u}'(R_y) = 0. \tag{A 5}$$

Appendix B. Linearization of constitutive equation

The invariants of the rate of strain in (2.6) can be expressed in cylinder coordinates as

$$\dot{\gamma} = \sqrt{\tfrac{1}{2}\left(\dot{\gamma}_{rr}^2 + \dot{\gamma}_{\theta\theta}^2 + \dot{\gamma}_{zz}^2\right) + \dot{\gamma}_{r\theta}^2 + \dot{\gamma}_{rz}^2 + \dot{\gamma}_{z\theta}^2}, \tag{B 1}$$

whose reciprocal can be expanded about the basic flow as

$$\dot{\gamma}^{-1} = \bar{\dot{\gamma}}^{-1} - \tfrac{1}{2}\bar{\dot{\gamma}}^{-3}[(\bar{\dot{\gamma}}_{rr}\dot{\gamma}'_{rr} + \bar{\dot{\gamma}}_{\theta\theta}\dot{\gamma}'_{\theta\theta} + \bar{\dot{\gamma}}_{zz}\dot{\gamma}'_{zz}) + 2(\bar{\dot{\gamma}}_{r\theta}\dot{\gamma}'_{r\theta} + \bar{\dot{\gamma}}_{zr}\dot{\gamma}'_{zr} + \bar{\dot{\gamma}}_{z\theta}\dot{\gamma}'_{z\theta})] + O(\dot{\gamma}'), \tag{B 2}$$

where $\bar{\dot{\gamma}} = \sqrt{\tfrac{1}{2}(\bar{\dot{\gamma}}_{rr}^2 + \bar{\dot{\gamma}}_{\theta\theta}^2 + \bar{\dot{\gamma}}_{zz}^2) + \bar{\dot{\gamma}}_{r\theta}^2 + \bar{\dot{\gamma}}_{rz}^2 + \bar{\dot{\gamma}}_{z\theta}^2}$ is the second invariant of the rate-of-strain of the basic flow. The linearized form of (B 2) is

$$\dot{\gamma}^{-1} = \bar{\dot{\gamma}}^{-1} + \dot{\gamma}'^{-1}, \tag{B 3}$$

and $\dot{\gamma}'^{-1} = -\tfrac{1}{2}\bar{\dot{\gamma}}^{-3}[(\bar{\dot{\gamma}}_{rr}\dot{\gamma}'_{rr} + \bar{\dot{\gamma}}_{\theta\theta}\dot{\gamma}'_{\theta\theta} + \bar{\dot{\gamma}}_{zz}\dot{\gamma}'_{zz}) + 2(\bar{\dot{\gamma}}_{r\theta}\dot{\gamma}'_{r\theta} + \bar{\dot{\gamma}}_{zr}\dot{\gamma}'_{zr} + \bar{\dot{\gamma}}_{z\theta}\dot{\gamma}'_{z\theta})]$. The linearized constitutive equation is derived by substitution of (B 3) into (2.6). It is

$$\tau_{ij} = \bar{\tau}_{ij} + \tau'_{ij}. \tag{B 4}$$

The expressions for each component are

$$\tau'_{rr} = \left(1 + \frac{\tau_0}{\bar{\dot{\gamma}}}\right)\gamma'_{rr} - \frac{\tau_0}{2\bar{\dot{\gamma}}^3}[(\bar{\dot{\gamma}}_{rr}\dot{\gamma}'_{rr} + \bar{\dot{\gamma}}_{\theta\theta}\dot{\gamma}'_{\theta\theta} + \bar{\dot{\gamma}}_{zz}\dot{\gamma}'_{zz}) + 2(\bar{\dot{\gamma}}_{r\theta}\dot{\gamma}'_{r\theta} + \bar{\dot{\gamma}}_{zr}\dot{\gamma}'_{zr} + \bar{\dot{\gamma}}_{z\theta}\dot{\gamma}'_{z\theta})]\bar{\dot{\gamma}}_{rr}, \tag{B 5a}$$

$$\tau'_{\theta\theta} = \left(1 + \frac{\tau_0}{\bar{\dot{\gamma}}}\right)\gamma'_{\theta\theta} - \frac{\tau_0}{2\bar{\dot{\gamma}}^3}[(\bar{\dot{\gamma}}_{rr}\dot{\gamma}'_{rr} + \bar{\dot{\gamma}}_{\theta\theta}\dot{\gamma}'_{\theta\theta} + \bar{\dot{\gamma}}_{zz}\dot{\gamma}'_{zz}) + 2(\bar{\dot{\gamma}}_{r\theta}\dot{\gamma}'_{r\theta} + \bar{\dot{\gamma}}_{zr}\dot{\gamma}'_{zr} + \bar{\dot{\gamma}}_{z\theta}\dot{\gamma}'_{z\theta})]\bar{\dot{\gamma}}_{\theta\theta}, \tag{B 5b}$$

$$\tau'_{zz} = \left(1 + \frac{\tau_0}{\bar{\dot{\gamma}}}\right)\gamma'_{zz} - \frac{\tau_0}{2\bar{\dot{\gamma}}^3}[(\bar{\dot{\gamma}}_{rr}\dot{\gamma}'_{rr} + \bar{\dot{\gamma}}_{\theta\theta}\dot{\gamma}'_{\theta\theta} + \bar{\dot{\gamma}}_{zz}\dot{\gamma}'_{zz}) + 2(\bar{\dot{\gamma}}_{r\theta}\dot{\gamma}'_{r\theta} + \bar{\dot{\gamma}}_{zr}\dot{\gamma}'_{zr} + \bar{\dot{\gamma}}_{z\theta}\dot{\gamma}'_{z\theta})]\bar{\dot{\gamma}}_{zz}, \tag{B 5c}$$

$$\tau'_{r\theta} = \left(1 + \frac{\tau_0}{\bar{\dot{\gamma}}}\right)\gamma'_{r\theta} - \frac{\tau_0}{2\bar{\dot{\gamma}}^3}[(\bar{\dot{\gamma}}_{rr}\dot{\gamma}'_{rr} + \bar{\dot{\gamma}}_{\theta\theta}\dot{\gamma}'_{\theta\theta} + \bar{\dot{\gamma}}_{zz}\dot{\gamma}'_{zz}) + 2(\bar{\dot{\gamma}}_{r\theta}\dot{\gamma}'_{r\theta} + \bar{\dot{\gamma}}_{zr}\dot{\gamma}'_{zr} + \bar{\dot{\gamma}}_{z\theta}\dot{\gamma}'_{z\theta})]\bar{\dot{\gamma}}_{r\theta}, \tag{B 5d}$$

$$\tau'_{z\theta} = \left(1 + \frac{\tau_0}{\bar{\dot{\gamma}}}\right)\gamma'_{z\theta} - \frac{\tau_0}{2\bar{\dot{\gamma}}^3}[(\bar{\dot{\gamma}}_{rr}\dot{\gamma}'_{rr} + \bar{\dot{\gamma}}_{\theta\theta}\dot{\gamma}'_{\theta\theta} + \bar{\dot{\gamma}}_{zz}\dot{\gamma}'_{zz}) + 2(\bar{\dot{\gamma}}_{r\theta}\dot{\gamma}'_{r\theta} + \bar{\dot{\gamma}}_{zr}\dot{\gamma}'_{zr} + \bar{\dot{\gamma}}_{z\theta}\dot{\gamma}'_{z\theta})]\bar{\dot{\gamma}}_{z\theta}, \tag{B 5e}$$

$$\tau'_{rz} = \left(1 + \frac{\tau_0}{\bar{\dot{\gamma}}}\right)\gamma'_{rz} - \frac{\tau_0}{2\bar{\dot{\gamma}}^3}[(\bar{\dot{\gamma}}_{rr}\dot{\gamma}'_{rr} + \bar{\dot{\gamma}}_{\theta\theta}\dot{\gamma}'_{\theta\theta} + \bar{\dot{\gamma}}_{zz}\dot{\gamma}'_{zz}) + 2(\bar{\dot{\gamma}}_{r\theta}\dot{\gamma}'_{r\theta} + \bar{\dot{\gamma}}_{zr}\dot{\gamma}'_{zr} + \bar{\dot{\gamma}}_{z\theta}\dot{\gamma}'_{z\theta})]\bar{\dot{\gamma}}_{rz}. \tag{B 5f}$$

Substituting basic flow and the relation between the strain and velocity into (B 5), it follows that

$$\tau'_{rr} = \left(1 + \frac{\tau_0}{\bar{\dot{\gamma}}}\right)\tau'_{rr},\ \tau'_{\theta\theta} = \left(1 + \frac{\tau_0}{\bar{\dot{\gamma}}}\right)\gamma'_{\theta\theta},\ \tau'_{zz}\left(1 + \frac{\tau_0}{\bar{\dot{\gamma}}}\right)\gamma'_{zz},\ \tau'_{z\theta} = \left(1 + \frac{\tau_0}{\bar{\dot{\gamma}}}\right)\gamma'_{z\theta}, \quad \text{(B 6}a\text{)}$$

$$\tau'_{r\theta} = \left(1 + \frac{\tau_0}{\bar{\dot{\gamma}}}\right)\gamma'_{r\theta} - \frac{\tau_0}{\bar{\dot{\gamma}}^3}(\bar{\dot{\gamma}}_{r\theta}\dot{\gamma}'_{r\theta} + \bar{\dot{\gamma}}_{zr}\dot{\gamma}'_{zr})\bar{\dot{\gamma}}_{r\theta}, \quad \text{(B 6}b\text{)}$$

$$\tau'_{rz} = \left(1 + \frac{\tau_0}{\bar{\dot{\gamma}}}\right)\gamma'_{rz} - \frac{\tau_0}{\bar{\dot{\gamma}}^3}(\bar{\dot{\gamma}}_{r\theta}\dot{\gamma}'_{r\theta} + \bar{\dot{\gamma}}_{zr}\dot{\gamma}'_{zr})\bar{\dot{\gamma}}_{rz}, \quad \text{(B 6}c\text{)}$$

Thus, equation (B 6*a*)–(B 6*c*) lead directly to (3.10*a*)–(3.10*c*).

REFERENCES

Ali, M. E. & Weidman, P. D. 1993 On the linear stability of cellular spiral Couette flow. *Phys. Fluids* A **5**, 1188–1199.

Al-Mubaiyedh, U. A., Sureshkumar, R. & Khomami, B. 2000 Linear stability of viscoelastic Taylor–Couette flow: influence of fluid rheology and energetics. *J. Rheol.* **44**, 1121–1138.

Avgousti, M. & Beris, A. N. 1993 Non-axisymmetric modes in the viscoelastic Taylor–Couette flow. *J. Non-Newtonian Fluid Mech.* **50**, 225–251.

Beris, A. N., Tsamopouos, J. A., Armstrong, R. C. & Brown, R. A. 1985 Creeping motion of a sphere through a Bingham plastic. *J. Fluid Mech.* **158**, 219–244.

Bird, R. B., Amstrong, R. C. & Hassager, O. 1977 *Dynamics of Polymeric Liquids*. John Wiley.

Bird, R. B., Dai, G. C. & Yarusso, B. J. 1983 The rheology and flow of viscoplastic material. *Rev. Chem. Engng* **1**, 1–70.

Canuto, C., Hussaina, M. Y., Quarteront, A. & Zang, T. A. 1988 *Spectral Methods in Fluid Dynamics*. Springer.

Cheng, F. & Chang, M. H. 1992 Stability of Taylor–Dean flow in a small gap between rotating cylinders. *J. Fluid Mech.* **243**, 443–455.

Coronado, O., Souza, M. P. R. & Carvalho, M. S. 2002 Taylor–Couette instability of viscoplastic liquids. *74th Society of Rheology Annual Meeting, Minneapolis, Minnesota, October 13–18, 2002.*

Cui, H. Q. & Liu, X. S. 1995 Research on helical flow of non-Newtonian fluids in eccentric annuli *SPE 29940. Proc. Intl. Meeting on Petroleum Enging, Beijing, China.*

Diprima, R. C. & Swinney, H. L. 1981 Instability and transition in flow between concentric rotating cylinders. In *Hydrodynamic Instabilities and the Transition to Turbulence*. Springer.

Frigaard, I. A., Howison S. D. & Sobey I. J. 1994 On the stability of Poiscuille flow of a Bingham fluid. *J. Fluid Mech.* **263**, 133–150.

Garbow, B. S. 1978 Algorithm 535: the QZ algorithm to solve the generalized eigenvalue problem for complex matrices. *ACM Trans. Math. Software* **4**, 404–410.

Graebel, P. G. 1962 The hydrodynamic stability of a Bingham fluid in Couette flow. *Intl Symp. on 2nd Order Effects in Elasticity, Plasticity and Fluid Dynamics, Haifa*, pp. 636–649, Pergamon.

Gupta, G. K. 1999 Hydrodynamic stability of the plane Poiseulle flow of an electrorheological fluid. *Intl J. Non-Linear Mech.* **34**, 589–602.

Hu, H. C. & Kelly, R. E. 1995 Effect of a time-periodic axial shear flow upon the onset of taylor vortices. *Phys. Rev.* E **51**, 3242–3251.

Hung, W. L., Joseph, D. D. & Munson, B. R. 1972 Global stability of spiral flow. Part 2. *J. Fluid Mech.* **51**, 593–612.

Joo, Y. L. & Shaqfeh, E., S., G. 1992 A purely elastic instability in Dean and Taylor–Dean flow. *Phys. Fluids* A **4**, 524–542.

Joo, Y. L. & Shaqfeh, E. S. G. 1994 Observations of purely elastic instabilities in the Taylor–Dean flow of a Boger fluid. *J. Fluid Mech.* **262**, 27–73.

Joseph, D. D. & Munson, B. R. 1970 Global stability of spiral flow. *J. Fluid Mech.* **43**, 545–575.

Kiessling, I. 1963 Uber das Taylorsche Stabilitatsproblem bei zusatzlicher axialer Durchstromung der Zylinder. *Duetsche Versuchsanstalt fur Luft-Unraumfahrt Bericht* 290.

Larson, R. G. 1992 Instabilities in viscoelastic flows. *Rheol. Acta* **31**, 213–263.

Larson, R. G. Shaqfeh, E. S. G. & Muller, S. J. 1990 A purely elastic instability in Taylor–Couette flow. *J. Fluid Mech.* **218**, 573–600.

Luo, Y. & Peden, J. M. 1990 Laminar annular helical flow of power-law fluids. Part 1: Various profiles and axial flow rates. *SPE 20304*.

Ludwieg, H. 1964 Experimentelle Nachprufung des stabilitatstheorien fur reibungsfreie Stromungen mit schraubenlinienformigen stromlinien. *Z. Flugwiss.* **12**, 304–309.

Mcfadden, G. B., Coriell, S. R., Murray, B. T., Glichsman, M. E. & Selleck, M. E. 1990 Effect of a crystal-melt interface on Taylor-vortex flow. *Phys. Fluids* A **2**, 700–705.

Marques, F. & Lopez, J. M. 1997 Taylor–Couette flow with Axial oscillations of the inner cylinder: Floquet analysis of the basic flow. *J. Fluid Mech.* **348**, 153–175.

Meseguer, A. & Marques, F. 2000 On the competition between centrifugal and shear instability in spiral Couette flow. *J. Fluid Mech.* **402**, 33–56.

Moser, R. D., Moin, P. & Leonard, A. 1983 A spectral numerical method for the Navier–Stokes equations with applications to Taylor–Couette flow. *J. Comput. Phys.* **52**, 524–544.

Mott, J. E. & Joseph, D. D. 1968 Stability of parallel flow between concentric cylinders. *Phys. Fluids* **11**, 2065–2073.

Muller, S. J., Larson, R. G. & Shaqfeh, E. S. 1989 A purely elastic transition in Taylor–Couette flow. *Rheol. Acta* **28**, 499–503.

Muller, S. J., Shaqfeh, E. S. G. & Larson, R. G. 1993 Experimental studies of the onset of oscillatory instability in viscoelastic Taylor–Couette flow. *J. Non-Newtonian Fluid Mech.* **46**, 315–330.

Nouar, C. & Frigaard, I. A. 2001 Nonlinear stablity of Poiseuille flow of Bingham fluid: theoretical results and comparison with phenomenological criteria. *J. Non-Newtonian Fluid Mech.* **100**, 127–149.

Nsom, B. 1996 Stability of fiber suspension flow in curved channel. *J. Phys.* II *Paris* **6**, 1483–1492.

Nsom, B. 1998 Stability of Taylor–Dean flow of fiber suspension. *Appl. Mech. Engng* **3**, 185–204.

Nsom, B. & Mangel, H. 2001 Stability of Taylor–Dean flow of Bingham fluid. *12th Intl Couette–Taylor Workshop, Evanston, USA, September 6–8, 2001*.

Oldroyd, J. G. 1947 A rational formulation of the equations of plastic flow for a Bingham solid. *Proc. Camb. Phil. Soc.* **43**, 100–105.

Ollis, D. F. Pelizzetti, E. & Serpone, N. 1991 Photocatalyzed destruction of water/contaminants. *Environ. Sci. Technol.* **25**, 1523–1529.

Orszag, S. A. 1971 Accurate solution of the Orr–Sommerfeld stability equation. *J. Fluid Mech.* **50**, 689–703.

Pascal, J. P. & Rasmussen, H. 1995 Stability of power-law fluid-flow between rotating cylinders. *Dyn. Stab. Sys.* **10**(1), 65–93.

Renardy, M., Renardy, Y., Sureshkumar, R. & Beris, A. N. 1990 Hopf–Hopf and steady Hopf mode interactions in Taylor–Couette flow of an upper convected Maxwell liquid. *J. Non-Newtonian Fluid Mech.* **63**, 1–31.

Shaqfeh, E. S. G. 1996 Purely clastic instabilities in viscometric flows. *Annu. Rev. Fluid Mech.* **28**, 129–185.

Simon, H. B. & Ole, H. 1992 Flow of viscoplastic fluid in a rotating concentric annulus. *J. Non-Newtonian Fluid Mech.* **42**, 19–36.

Sparrow, E. M., Munro, W. D. & Jonsson, V. K. 1964 Instability of the flow between rotating cylinders: the wide-gap problem. *J. Fluid Mech.* **20**, 35–46.

Tadmor, Z. & Bird, R. B. 1974 Rheological analysis of stabilizing forces in wire-coating dies. *Polymer. Engng. Sci.* **14**, 124–136.

Weisberg, A. Y., Smits, A. & Keverkidis, I. 1997 Delaying transition in Taylor–Couette flow with axial motion of the inner cylinder. *J. Fluid Mech.* **348**, 141–151.